Combined Geometric-Radiometric and Neural Network Approach to Shallow Bathymetric Mapping with UAS Imagery

*Richard K. Slocum[1], Christopher E. Parrish[1], Chase H. Simpson[1]

[1]School of Civil and Construction Engineering, Oregon State University, 101 Kearney Hall, 1491 SW Campus Way, Corvallis, OR 97331, USA

*Corresponding Author: Richard K Slocum, slocumr@oregonstate.edu

Keywords

UAS; SfM; SDB; Bathymetry; Neural Network

Abstract

There is a pressing need for shallow bathymetry in regions around the world, including in fragile marine ecosystems, such as coral reefs. Unfortunately, mapping these shallow-water areas using *in situ* or boat-based methods is expensive, time consuming, and potentially dangerous, due to the need to put personnel and/or boats in high-energy nearshore areas, which may contain rocks, reefs, and other submerged hazards. For this reason, passive remote sensing methods of shallow bathymetric mapping have been rapidly growing in interest and usage. Two general categories of approaches using passive imaging can be distinguished as: 1) those based on geometry (stereo-photogrammetry); 2) those based on radiometry (attenuation of light in the water column). These two broad categories of approaches have been tested on imagery collected using aircraft and satellites in numerous previous studies. Recent work within the geometric category includes processing unmanned aircraft system (UAS) imagery using Structure from Motion and Multi-View Stereo (SfM-MVS) photogrammetry, while radiometric methods encompass the broad range of spectral bathymetry retrieval algorithms. Each broad approach category has advantages and disadvantages. Fortunately, the geometric and radiometric approaches are highly complementary. The geometric approaches tend to work best in areas of high bottom texture, which facilitates feature matching in the SfM-MVS software. Meanwhile, the radiometric approaches work best in relatively homogeneous bottom types. To leverage the strengths of each type of approach and overcome their respective weaknesses, this work develops and tests a combined geometric-radiometric bathymetric mapping approach designed for shallow-water mapping from UAS imagery. Four radiometric models of varying complexity are tested, ranging from a color-based lookup table approach to neural networks. Two UAS flights on Buck Island, off St Croix in the U.S. Virgin Islands (USVI), are used to assess the accuracy of the methodology when compared to aerial bathymetric lidar data. The results show that the combined geometric-radiometric approach provides an increase in spatial coverage of up to 61% and improvement (i.e. decrease) in 95th percentile error of up to 49% when compared to traditional refraction-corrected SfM-MVS bathymetry.

1. Introduction

There is a persistent need for bathymetric data in shallow coastal regions around the world. These bathymetric data are critical in modeling inundation from coastal storms and sea level rise, monitoring fragile marine ecosystems (e.g., coral reef habitats), supporting coastal engineering and coastal resilience initiatives, and informing coastal management decisions (Miller et al., 2011; Leon et al., 2013; Harris 1972; Harris 2012). Cost- and time- efficient remote sensing methods of shallow bathymetric mapping are of growing interest due to the vastness and, in many cases, remoteness of coastal areas around the globe in which shallow bathymetry is entirely lacking, and the immense resources that would be required to map them with sonar (Board, 2004; IHO, 2018; Forfinski-Sarkozi and Parrish, 2019).

The ability to estimate bathymetry via spectral characteristics of airborne or satellite imagery is documented at least as far back as the 1970s (Lyzenga, 1978), and techniques for bathymetry retrieval from imagery have proliferated rapidly with the increasing availability of moderate-resolution satellite imagery, such as from Landsat 8 Operational Land Imagery and Sentinel-2 Multispectral Instrument, as well as commercial high-resolution satellite imagery (Legleiter et al. 2004, 2009; Lyzenga et al. 2006). The techniques for bathymetry retrieval from passive, optical imagery are often broadly referred to as spectrally derived bathymetry (SDB). SDB algorithms are highly varied, with some being more theory-based and others purely empirical. However, a common denominator is that most, if not all, are based on the wavelength-dependent exponential attenuation of light in the water column, which is generally modeled with the Beer-Lambert Law (Lyzenga 1978, 1981). It is this broad class of algorithms that we refer to in this paper as "radiometric" bathymetry retrieval techniques.

Meanwhile, a fundamentally different approach to mapping bathymetry from remotely-sensed imagery is based on geometry, rather than radiometry. The origins of this geometric approach lie in photobathymetry, which was used first discussed in the 1940s (Rinner, 1948), and implemented in the 1960s (Tweinkel 1963, Meijer 1964) to map bathymetry from overlapping stereo imagery using photogrammetric procedures, modified to account for refraction at the air-water interface (Collins, 1979; Brewer, 1979). A much more recent—although not fundamentally dissimilar—geometric approach uses structure from motion (Schöneberger, 2016) and multi-view stereopsis (Hirschmuller 2007, Rothermel et al. 2012) (SfM-MVS). SfM-MVS algorithms employ the same photogrammetric principles, but incorporate algorithms from the computer vision community. UAS-based SfM-MVS mapping is now commonly used for geoscience applications due to the relatively low cost, ability to rapidly mobilize to perform a survey, higher spatial resolution compared to satellite based methods, and the suitability for repeated mapping (Westoby 2012; Fonstad 2013). Just as in conventional photobathymetry, SfM-MVS bathymetry generally requires *a posteriori* refraction correction, as the underlying techniques were designed for subaerial (i.e., above-water), rather than subaqueous mapping. A few widely-used approaches to refraction correction from SfM-MVS bathymetry are: 1) processing data without accounting for refraction, and using a constant scale factor to correct depths (Woodget et al. 2015), 2) processing data without accounting for refraction, and estimating a mean depth correction for each point based on a refraction model (Dietrich 2017), 3) processing data with a bundle adjustment which does account for refraction in a multimedia bundle adjustment (Maas 2015; Kotowski 1988; Murase et al. 2008; Mulsow et al. 2018) followed by a dense reconstruction which also accounts for refraction (Mandlburger 2019).

Individually, both the radiometric approaches (i.e., SDB) and geometric approaches (stereo-photogrammetry) have strengths and weaknesses. Fortunately, the geometric and radiometric approaches are highly complementary, such that the strengths of each can overcome the weaknesses of the other. Specifically, geometric approaches work well when the bottom is sufficiently textured to enable feature matching, whereas radiometric approaches tend to work well in areas of relatively homogeneous substrate and uniform water clarity. Recent work by Starek and Giessel (2017) demonstrated a step towards a

hybrid approach to perform a UAS bathymetric inversion by using a SfM-MVS derived orthophoto regressed against *in-situ* depth measurements surveyed using GNSS.

The aim of this study is to test a novel geometric-radiometric fusion method to map bathymetry using radiometric modeling of each image captured from a UAS, without the need for an *in-situ* survey. The results from the geometric processing (i.e., dense point cloud, camera exterior and interior orientations) are used to train a radiometric (i.e., spectrally-based) approach that estimates depths from multiple spectral bands. Four different radiometric methods are tested for the prediction, including a red, green, blue (RGB) lookup table, a log-ratio based approach (similar to a number of widely-used SDB algorithms), and two machine learning approaches using neural networks with different input feature sets. The results are tested using UAS imagery collected over a project site in the U.S. Virgin Islands (USVI) and compared against a bathymetric lidar dataset. The results show that for each of the radiometric models tested, the combined geometric-radiometric approach improves spatial coverage and reduces error (specifically, the 95th percentile error, determined by differencing the modeled bathymetry and reference bathymetry).

This manuscript is organized as follows: Section 2 provides an overview of the geometric-radiometric methodology. A general overview of the methodology is included, with further details provided in the following subsections. Section 3 described the field site, experiment design, and reference dataset. Section 4 presents results from the methodology, which are then discussed in Section 5. Section 6 summarizes the findings in a conclusion.

2. Methods

The geometric-radiometric methodology introduced here, and depicted in Figure 1, corrects bathymetric SfM-MVS data to account for refraction while simultaneously leveraging radiometric methods to provide continuous data, even in regions where SfM-MVS methods were unable to resolve depths. The first two steps, the acquisition of overlapping RGB imagery and processing of the data with SfM-MVS software, are considered as “pre-processing” steps for this study, and are not addressed in detail here. However, it is important to note that it is critical to collect high-quality imagery and to generate accurate results using SfM-MVS software. Detailed recommendations and procedures for completing Steps 1 and 2 can be found in the literature, notably Maas 2015, Mandlburger 2019, Slocum et al. 2020. Very briefly, it is important to use a UAS which utilizes real time kinematic (RTK) or post-processed kinematic (PPK) GNSS and to collect data under conditions of clear water, varying seafloor texture (i.e., not a homogeneous sandy bottom), low wave height, minimal relict foam from breaking waves, and minimal sun glint. Data for this study were processed using Agisoft PhotoScan, which has subsequently been renamed Metashape (Agisoft, 2018), with the alignment settings set to “high” and dense reconstruction setting also set to “high.”

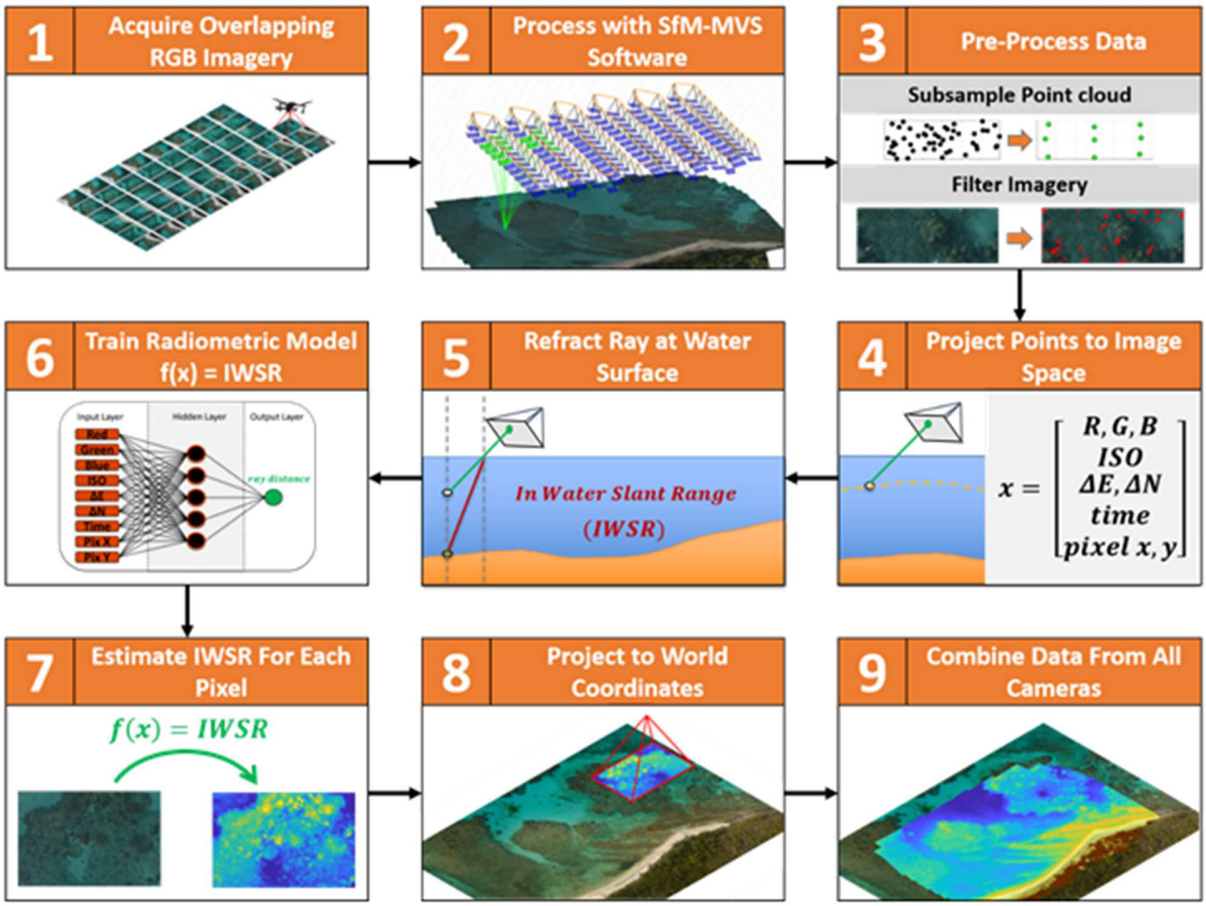

Figure 1. Geometric-radiometric workflow developed and tested in this study.

The dense point cloud, camera exterior orientation, and camera interior orientation are computed in Step 2. In Step 3, the point cloud is subsampled to ensure a uniform spatial distribution and the raw imagery is filtered to remove specular reflections using an intensity threshold. In Step 4, each point in the subsampled point cloud is projected into the camera image coordinates, and the red, green, and blue digital numbers are computed. Note that refraction is not accounted for here as the SfM-MVS processing in Step 2 did not account for refraction. The camera ISO, relative position from the camera to the point, time the image was acquired at, and pixel coordinates are also recorded. These variables comprise the independent variables used to train the radiometric model. The in-water slant range (IWSR), or distance of the underwater portion of the optical ray from the refraction corrected point to the water surface, is computed in Step 5 as the dependent variable for the radiometric model. The IWSR is computed using Snell's law to refract the ray at the water surface and makes the simplifying assumption that there is no horizontal shift of the point (see further discussion below). The radiometric model is trained in Step 6. Note that a neural network is depicted in this subfigure, but four different radiometric models were tested for this step. In Step 7, the same independent variables that were computed in Step 4 are now computed for each pixel in image space. The radiometric model trained in Step 6 is used to estimate an IWSR for each pixel. In Step 8, the IWSR is converted to world coordinates by performing ray tracing and refracting the ray at the air water interface. Step 9 merges estimated depths from every camera into a combined DEM or point cloud.

The results of the SfM-MVS processing in Step 2, as well as a mean water surface elevation estimated from a local tide gauge, were used to train a radiometry-based model which estimates the water depth based on the camera interior and exterior orientation and RGB values of each image. The radiometric model was used to estimate depths for every pixel in every image, resulting in final depth estimates, regardless of bottom texture. Four different models were tested, each using different methods, features, and levels of complexity.

The data were first preprocessed to downsample the point cloud and remove specular solar reflections from the imagery. The subsampled point cloud was then projected into each of the images, and nine features were computed for each projection. Using the estimated water surface, the ray was then refracted at the water surface and the in-water slant range (IWSR), defined as the distance from the water surface to the predicted 3D point (based on the SfM-MVS results), was computed. A model was then trained, which predicts the IWSR as a function of the features computed in the previous step. Using this model, an IWSR value was computed for each pixel in each image. This IWSR was used to compute the world coordinates using the estimated water surface elevation and accounting for refraction at the air-water interface. This was performed for each image, and the data were combined and filtered to produce a final bathymetric point cloud and/or digital surface model.

2.1 Subsample Point Cloud (Step 3a)

The results from SfM-MVS processing often consist of a dense matching point cloud with tens of millions of points, which can be computationally expensive in further processing steps. In order to facilitate subsequent processing, in Step 3a, the point cloud was sub-sampled using the CloudCompare spatial subsampling tool, which ensures a minimum, specified separation of any two points in the output point cloud (CloudCompare, 2019). A value of 0.25 m was used as the minimum spacing between points in this research, yielding a point cloud with approximately 600,000 points, or 5% of the original points. Spatial filtering was selected, as opposed to random sampling, in an attempt to ensure that the data would be representative of the full variability of seafloor textures in the scene and not biased by regions of the point cloud with a higher point density. For this work, no outlier rejection was performed as a manual inspection of the point cloud data did not exhibit excessive noise. Additionally, as this dataset contained a portion of the area of interest (AOI) which was not underwater, data above the waterline were removed from the point cloud using an elevation threshold. These points above the water line were added back to the bathymetric data after processing to create a seamless topo-bathymetric surface.

2.2 Image Filtering (Step 3b)

Specular solar reflections (i.e., sun glint) and relict foam from small breaking waves were masked out of the raw imagery using an intensity-based filter. The RGB imagery was converted to the hue-saturation-value (HSV) color space, and a simple threshold was used to create a mask identifying pixels which contain a “value” (on the HSV scale) greater than 60%. This value is a representation of pixel brightness, and, in this study, was able to identify the bright specular returns in both datasets. The mask was expanded by 5 pixels in all dimensions to account for artifacts in the pixel values surrounding sun glint pixels, likely due to bleeding of oversaturated pixels and chromatic aberration.

The masked imagery was then convolved with a Gaussian smoothing kernel ($\sigma = 5$ pixels) to reduce any high-frequency noise in the imagery or artifacts from small-scale variability from ripples on the water surface. Artifacts on the edge of the imagery were minimized by padding the array values outside the image bounds with the nearest value in the image. Masked areas were omitted from the convolution, and

future processing steps omitted computing features or estimating depths for these masked regions. Examples of the image filtering steps are shown in Figure 2.

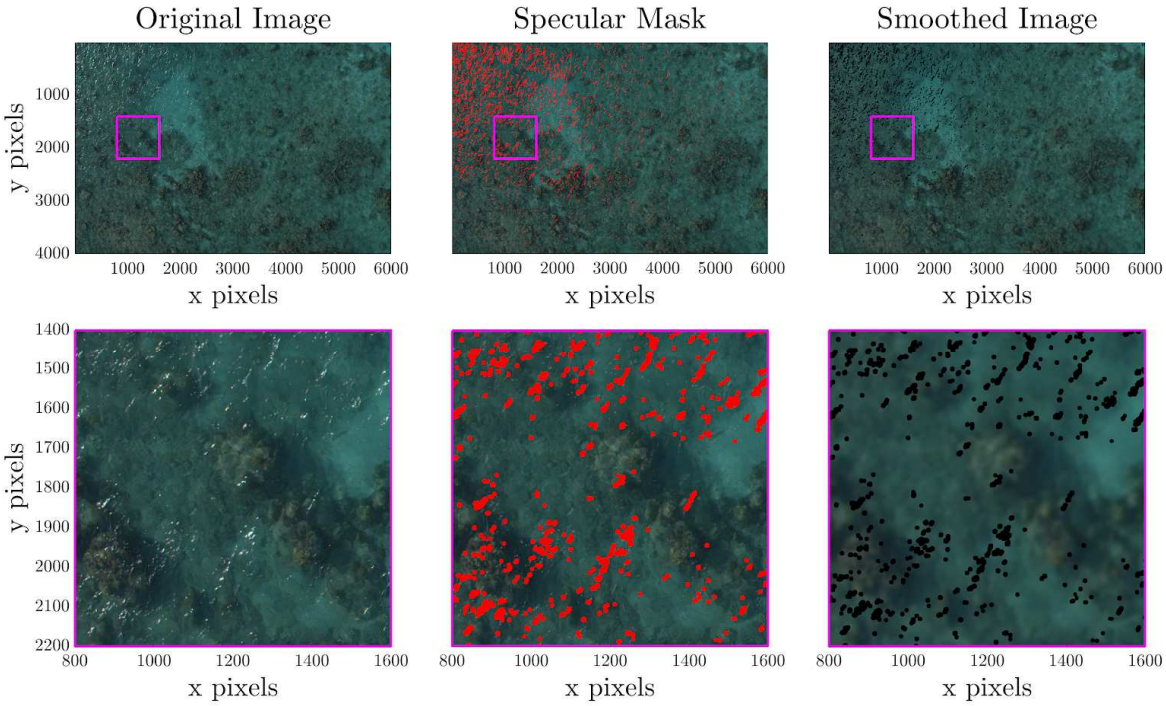

Figure 2. Specular reflections and bright, relict foam on the water surface are removed, then the image is smoothed with a Gaussian kernel.

2.3 Project Points to Image Space (Step 4 & 5)

Each point in the sub-sampled point cloud was projected into each image which captured that point within its field of view, and the following nine features were recorded: RGB digital numbers, image ISO, relative easting and northing from the camera to the point, pixel *x* and *y* coordinates, and time of image acquisition. Note that aperture and shutter speed were not included as they were held constant for the data acquisition. The nine features and the physical mechanism for potential ray-path induced variation in the RGB intensities are summarized in Table 1. The back projection of the points into the image plane did not incorporate any refraction at the air-water interface (Figure 3), since the SfM-MVS software used to generate the point cloud also did not account for refraction. The distance that the light travels from the point to the surface of the water is computed using a point with a refraction corrected depth. This refraction-corrected depth is computed using the same methodology as proposed in Dietrich, 2017, wherein it assumed that the horizontal translation of the point is negligible and the refraction of the light ray at the air water interface is computed using Snell's law and assuming a flat water surface. A diagram depicting the computation of the IWSR is shown in Figure 3. Note that this IWSR distance does not account for the distance the light has traveled to initially get to the seafloor. This simplifying assumption is due to the lack of additional data regarding the light incident on the water surface (e.g., direct sunlight, diffuse skylight, and reflections from clouds, nearby wave facets, etc.). The significance of this assumption should be investigated in future work.

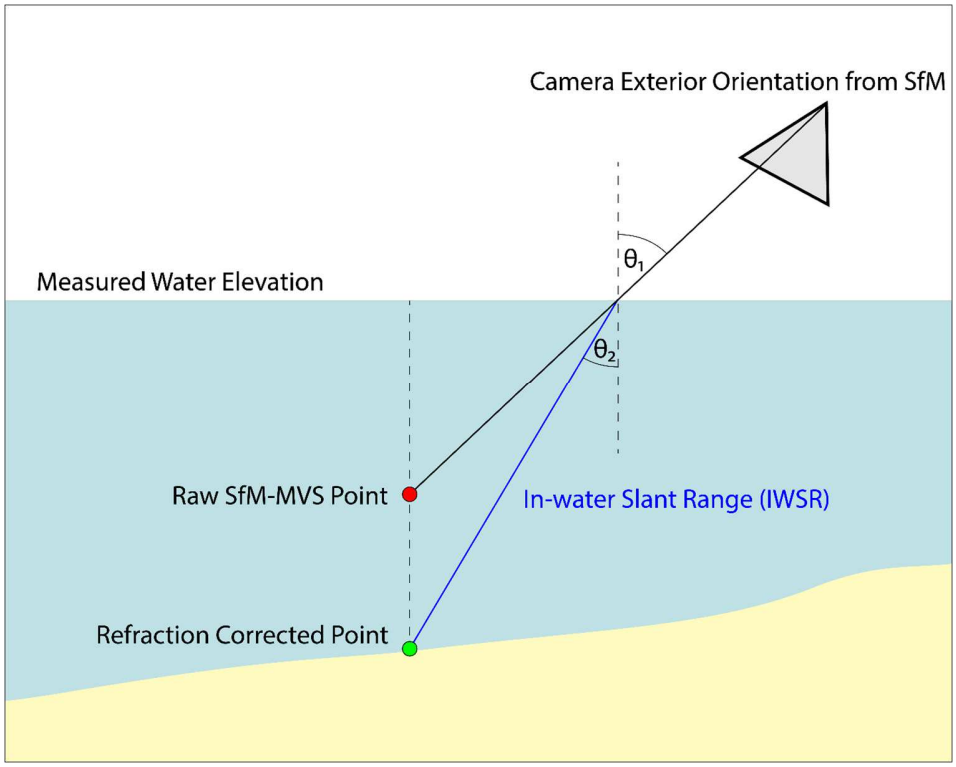

Figure 3. Points are projected into each image plane, and the IWSR is computed by accounting for refraction at the air-water interface.

Table 1. The nine features considered for use in a neural network.

Feature	**Induced variation in perceived depth due to:**
RGB Pixel Digital Numbers	The wavelength-dependent exponential attenuation of light in the water column (e.g., red attenuated more rapidly than blue)
Image ISO	Potentially-varying sensor gain of each image, and therefore image brightness
ΔE, ΔN (camera to point)	The incident angle dependence on light transmittance through the air water interface and the relative location of the sun inducing glare on the water surface
Pixel *x*, Pixel *y*	The lens artifacts causing portions of an image to be brighter than others (i.e. vignetting). Note that this could be omitted if the camera is pre-calibrated and corrected with a camera calibration.
Time	Temporally-varying environmental illumination, such as cloud cover or time of day. (Note: when used in conjunction with relative easting, northing and/or the pixel x, y coordinates, can theoretically identify images which experience cloud cover over only part of the image when using a complex model, such as a neural network. However, this parameter was found to be prone to overfitting of the data and should be used with caution.)

2.4 Train Model (Step 6)

The features described in Step 4 were used to train a model which was then used to predict the IWSR for every pixel in each image (Step 6). In this work, four different models were tested in this step, although any model which computes the IWSR as a function of these features could be used. The four different models were selected as a sampling of broad types of radiometric models and are not meant to represent all of the radiometric bathymetric models in the literature.

2.4.1 Model 1: RGB Lookup Table

The most simplistic model is an RGB lookup table, which assigns depth based on the mean of the values in the training dataset with the same color. This method utilizes a 3D lookup table, corresponding to the RGB channels of the imagery. Lookup tables have been used before for bathymetry retrieval from imagery, such as in Bowles et al. 2005. Imagery was acquired with variable ISO for this work, and was therefore normalized by dividing by the ISO value in order to convert the digital number recorded by the camera into a number that is more closely related to the number of photons received by the imaging sensor. Additionally, as this data was acquired in raw 14-bit format, the cell size of each bin in the 3D lookup table was set such that middle 99% of the normalized data in each channel was spread across 256 bins. (Finer vertical discretization could be achieved by increasing the bit depth, but 8-bits was found to provide sufficient vertical resolution for the shallow depth ranges covered in our study site.) The top and bottom 0.5% of the data were omitted as outliers. For each bin in the lookup table corresponding to a normalized RGB triplet, the mean values of the IWSRs of the training data were computed. The same normalization and binning was performed for new data with unknown IWSR distances, and the mean of the training data IWSR distances are assigned to the corresponding values.

2.4.2 Model 2: Ratio of Logs

The second method, loosely based on a common SDB algorithm (Stumpf et al., 2003), involves a linear transformation of the ratio of the logs of two channels of imagery, using transformation coefficients derived from a linear regression of reference depths on the ratio-of-logs. The Stumpf algorithm is generally implemented on radiance values (obtained through a radiometric calibration that converts from raw DNs to at-sensor radiance) or surface reflectance, obtained via an atmospheric correction algorithm, such as ACOLITE (Caballero and Stumpf, 2020; Vanhellemont and Ruddick, 2016). However, since this study used consumer-grade cameras on commercially-available UAS, without available radiometric response curves, and with imagery acquired from low altitudes under stable illumination conditions, the algorithm was instead implemented on raw image band digital numbers (DNs), after experimentally confirming that the use of raw DNs did not eliminate the existence of a strong linear relationship between reference depths and the ratio-of-logs. Another difference between most implementations of the Stumpf algorithm and our approach is that, while blue (B) and green (G) channels are typically used, due to providing the greatest depth penetration, we used the blue (B) and red (R) image bands. The original algorithm (Stumpf et al., 2003) does allow for other band combinations, besides (R) and (G), and, in this study, log(B)/log(R) was found to have a higher signal to noise ratio. The shallow (<4m) project site exhibited excellent water clarity, and the optical extinction of the red channel was not a concern. A linear fit was used to compute IWSR as a function of the ratio of the logs. Note that the assumption of a linear relationship may be negatively impacted by any strongly nonlinear response curve of the sensor, and is something that should be checked by anyone implementing our methods. For new data with unknown IWSRs, the ratio of the logs was computed, and the linear fit parameters were used to estimate the IWSR.

2.4.3 Model 3: Neural Network

The third method used a shallow neural network to train a regression model, which predicts the IWSR as a function of the input features. The neural network used for this work contained one hidden layer with 5 nodes, used Levenberg-Marquardt backpropagation, and was programmed using the MATLAB Deep Learning toolbox. The choice of 5 nodes and one hidden layer was made after qualitatively evaluating more simplistic and more complex topologies. More complex topologies tended to over-fit the training data, resulting in outliers propagating into the radiometric depth estimations, while more simplistic topologies with only a few nodes produced inaccurate results. While this neural network topology worked well for these experiments, it was considered beyond the scope of the study to investigate whether it would hold across different project sites or data sets. A *K*-fold ensemble of 10 models was used to train the data, using an 80-10-10 split of the data (e.g., 80% training data, 10% validation data, 10% testing data), and the mean of the models was used as the estimate of the IWSR. Two neural networks were tested in this work; one used just the RGB, and ISO data, while the other used all of the nine of the features described in Section 2.3.

2.5 Estimate Depth for Each Pixel in World Coordinates (Steps 7 & 8)

For every pixel in every image, a ray was projected into real world coordinates using a forward projection to a known elevation of the water surface (i.e. raytracing of image ray with a constant elevation water surface model). The refracted angle at the air water interface is computed using Snell's Law, with an estimated index of refraction of 1.00 and 1.34 for air and water, respectively. The IWSR is then projected through the water to real world coordinates.

2.6 Combine All Data (Step 9)

The point cloud depths of the same location on the seafloor varied between images ($\sigma \sim 0.5$ m), due to variability in the sea surface elevation and water surface normal vector due to waves, as is discussed in Fryer and Kniest (1985). Variability in the sea surface elevation produces perceived depths which are deeper or shallower than expected, due to variability in the true IWRD. Variability in the water surface normal vector results in horizontal and vertical positioning errors, due to the refraction at the air-water interface deviating from the predicted direction. These uncertainties were mitigated by computing a windowed average of the elevations in the final point cloud, which performed well, due to the overlapping imagery acquired for the SfM-MVS processing which ensured that each point on the seafloor was viewed multiple times from various angles. For this analysis, the final DEM was computed using a 10-cm cell size and computing a running average for the point cloud depths in each bin. Processing in this manner alleviated the need for storing the large point cloud in memory.

2.7 Geometric-Only Refraction Corrected Point cloud

A geometric-only point cloud is computed by correcting the SfM-MVS results using the methods described in Dietrich (2017). This point cloud is used to demonstrate the advantages of the geometric-radiometric methodology. Briefly, the same process is performed for each point in the point cloud. For each camera which captures that point within the viewing frustrum, a ray from that point to each camera is computed. Each ray is refracted using Snell's law, in the same way that is depicted in Figure 3 where horizontal translation of the point is assumed to be negligible, and a new estimated elevation is computed for each camera. The mean of these new elevations is used as the value for the corrected point cloud.

3. Experiment Design

The proposed methodology was assessed using data from two separate UAS missions on March 25, 2018, on the northwest end of Buck Island off of St Croix, USVI, USA. A custom UAS with a Sony A6300 camera and a carrier phase recording, Piksi Multi GNSS receiver was used to acquire nadir, 14-bit raw

imagery and raw GNSS observations at 10 Hz for SfM-MVS processing. Seven ground control points (GCPs) were surveyed with survey-grade (carrier-phase measuring, multi-constellation, multi-frequency receivers, paired with geodetic-quality antennas) GNSS and a 1" total station, and were used in the SfM-MVS processing. A bathymetric lidar dataset was acquired four months after the fieldwork and was used as the independent ground truth dataset for this study. Further discussion regarding the validity of the bathymetric lidar as a ground truth dataset given this large time gap is included in in Sections 3.5.2 and 5.4)

3.1 Field Site

The field site is approximately 300 m along-shore by 200 m cross-shore, as shown in Figure 4, with water depths of up to 4 m in the AOI. Approximately 20% of the field site encompasses the above-water topography of the northwest-facing, sandy beach. The beach is narrow (10-20 m) and backed by thick shrubs and hardwood trees farther inshore. The AOI is protected by an outer reef, and wave conditions were dominated by short period wind swell with amplitude less than 0.25 m. The seafloor is comprised of a variety of bottom types, including submerged coral, rock, seagrass, and sand. While water clarity was not directly measured, it was noted that the seafloor in water depths of greater than 10m was clearly visible in the areas surrounding the field site. The two missions were flown with a constant wind of approximately 15 mph (6.7 m/s) out of the NE between 4:45PM and 5:30PM local time, when the sun elevation ranged from 24° for the start of the first mission to 13° at the end of the last mission. There was intermittent cloud cover, which did affect the illumination of the field site during each of the missions. Buck Island and the surrounding waters are designated as a National Monument, and, therefore, all field work and UAS operations were performed with appropriate waivers, permits and certifications in a partnership with the United States National Park Service (NPS) and the National Oceanic and Atmospheric Administration (NOAA).

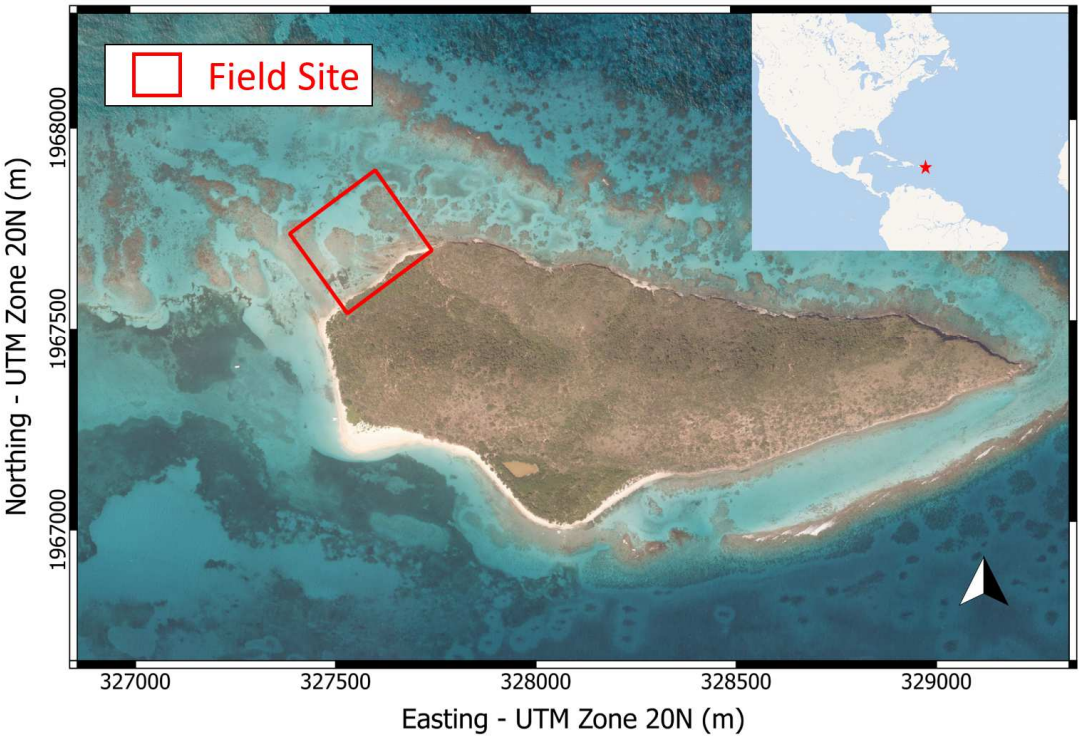

Figure 4. The project field site, shown by the red box, is located on the NW corner of Buck Island on St Croix, USVI.

3.2 UAS Specifications

A custom UAS, shown in Figure 5, built upon a DJI S900 airframe, was utilized for these missions. The autopilot, a 3DR Pixhawk, was used to trigger a Sony A6300 Camera with a 30-mm fixed focal length lens in order to acquire 14-bit RAW 24Mp RGB imagery (6000x4000). The Sony A6300 camera was installed on a 3D printed mount, which maintained a roughly nadir orientation. The primary GNSS for navigation used positions computed from code-ranging, L1 only measurements using the broadcast ephemeris. For mapping purposes, a Piksi GNSS receiver recorded raw carrier phase measurements and the timestamp of each camera exposure, triggered by the external flash of the camera, with a positional accuracy of approximately 3 cm horizontal, and 5 cm vertical. The maximum flight duration with the payload was approximately 12 minutes.

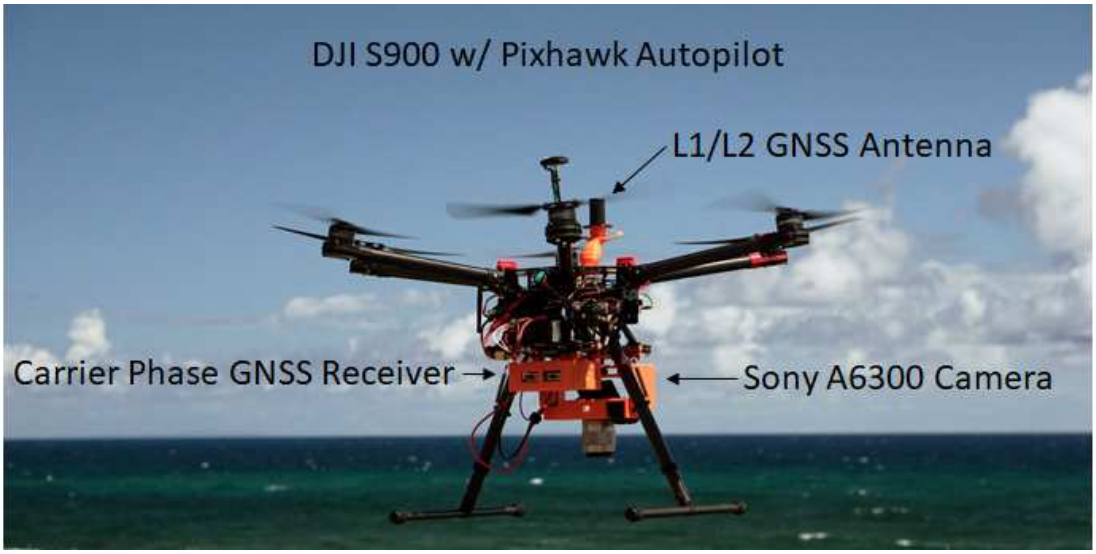

Figure 5. The S900 UAS used in this research.

3.3 UAS Mission Parameters

Two missions were flown over the same AOI at 100 m and 80 m altitudes and corresponding ground sampling distances of 13 mm and 10 mm, respectively. The 100 m mission acquired 154 images, while the 80 m mission acquired 252 images, with the flight lines depicted in Figure 6. Each mission required two flights and ~25 minutes to complete. The UAS was piloted manually for takeoff and landing, but flown in fully autonomous mode during mapping to capture imagery with 75% endlap and 75% sidelap at the water surface. Note that the effective endlap and sidelap on the seafloor increase with water depth. Missions were designed and monitored in real time via a 900MHz telemetry module using the Mission Planner software (Oborne, 2018). The Sony A6300 camera was set in manual mode, such that the shutter speed and aperture were fixed at 1/1000s and f/4, which acquired slightly underexposed imagery. In order to account for variability in illumination of the scene while ensuring the imagery was not overexposed, the ISO was set to auto-mode with an auto exposure value (EV) of -1. With these settings, the ISO ranged predominantly from 125 to 640, with a few images at ISO 800 and 1250 when clouds were present.

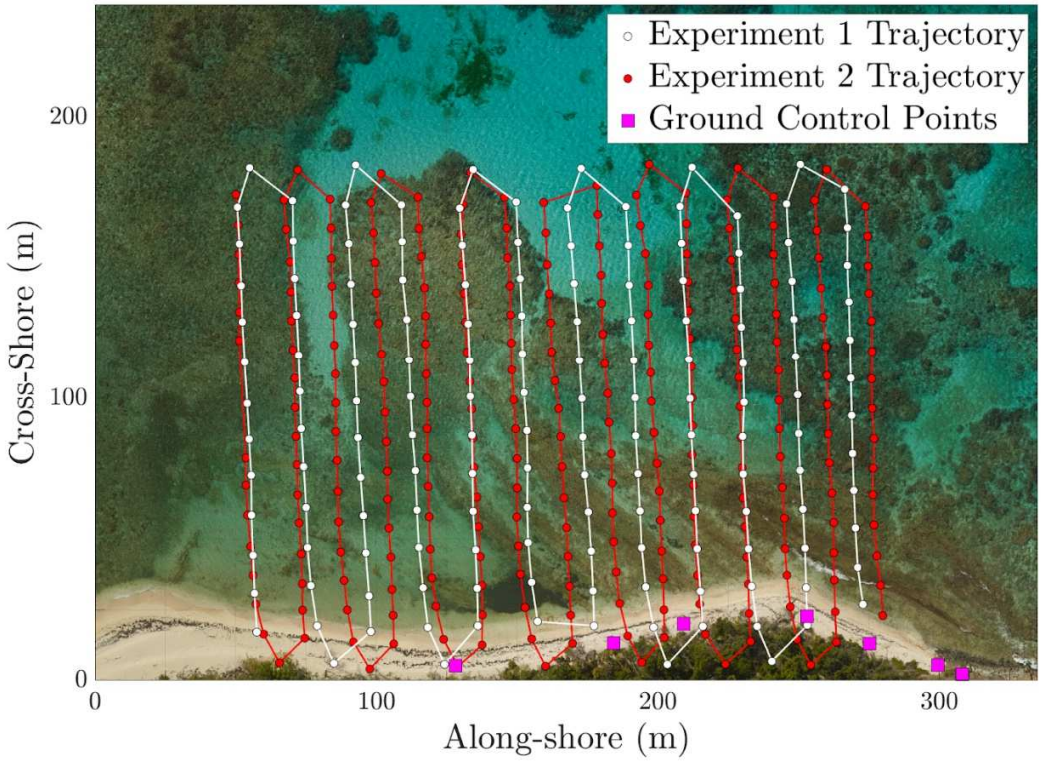

Figure 6. The flight trajectories, shown in arbitrary along-shore, cross-shore rectangular coordinates.

3.4 Ground Control Points

In order to constrain the SfM-MVS processing, seven 1m x 1m checkerboard patterned GCPs made of flexible PVC material were placed along the beach. The GCPs were placed such that they were evenly distributed across the alongshore extents of the AOI, and placed to maximize the cross-shore variability. Note that GCPs were not placed at the positions closest to the water or less than 100 m in the alongshore position, due to site-specific constraints. These GCPs were surveyed using a Leica TS15P 1" total station with a 360° prism on a monopod to an estimated accuracy of 2 cm.

3.5 Reference Data

3.5.1 Surveying Methods

A combination of total station, GNSS, and single-beam sonar was used to generate a reference bathymetric dataset and survey the GCPs. The reference data was only used to validate the ground truth bathymetric lidar dataset, while the GCPs were used in the SfM-MVS processing. All the data was converted to UTM Zone 20N (meters), NAD83 (2011) epoch 2010.00, with VIVD09 (Geoid 12B) orthometric heights. Two control points were occupied with static GNSS for over 2 hours each, and were processed with the NGS Online Positioning User Service (OPUS), once the precise ephemeris was available. The OPUS reported overall RMS for these points were 0.016 and 0.015 m. A Leica TS15P total station and a Leica 360° prism on a monopod were utilized to accurately measure all of the GCPs and

survey shallow bathymetry transects in relation to the control points positioned in the Static GNSS survey. Sonar data was acquired using a Hydrolite-TM echosounder and a Trimble R8-2 GNSS receiver mounted onto a Hobie Mirage tandem kayak. A second Trimble R8-2 GNSS antenna was set up as a base on one of the control points on shore to provide RTK positioning. The data were acquired in multiple transects running approximately parallel to shore at a sampling rate of 1 Hz.

3.5.2 Ground Truth

Bathymetric lidar data were acquired for St. Croix by the U.S. Army Corps of Engineers (USACE)–Joint Airborne Lidar Bathymetry Technical Center of Expertise (JALBTCX) on July 20, 2018, approximately four months after the UAS data acquisition, with a Teledyne Optech Coastal Zone Mapping and Imaging Lidar (CZMIL). The resultant point cloud contained an average data density of 6 pts/m^2.

The field site did not experience any major storms or large wave events in between the UAS data acquisition and the bathymetric lidar flight, though some erosion and accretion did occur along the beach. In order to assess the validity of using the bathymetric lidar data as a ground truth dataset for comparison with the UAS data throughout the AOI, the lidar data were compared to the reference data acquired at the time of the UAS survey. For each point in the reference dataset, the median elevation value from the lidar within a 1-m radius was used to compute the elevation difference. The comparison indicated a median difference of 12 cm between the lidar and the sonar and total station reference data for both topographic and bathymetric points, as shown in Figure 7. The 12-cm difference was subtracted from the lidar data so that it aligned with the reference data, as the reference data was used as ground control in the UAS processing. In general, the lidar data agrees well with the reference data, with 95% of the elevation differences (N=6764) fall between -0.22 m and 0.37 m (-0.34 m and 0.25 m after the 12-cm bias is removed). The spread of this distribution can be attributed to large gradients in elevation near the edges of the reef and near large coral heads and uncertainty in the surveyed reference dataset. There are outliers (greater than 0.5 m differences) near the shoreline (along-shore position 90 m - 140 m), which are attributed to areas of erosion and accretion in a few areas near the shoreline that occurred between the UAS survey and the lidar data acquisition. The implications of including this real erosion and accretion in the ground-truth dataset are discussed further in Section 5.4. Due to the substantially higher point density and greater coverage of the bathymetric lidar, it was ultimately selected as the ground-truth dataset to compare to the UAS depths.

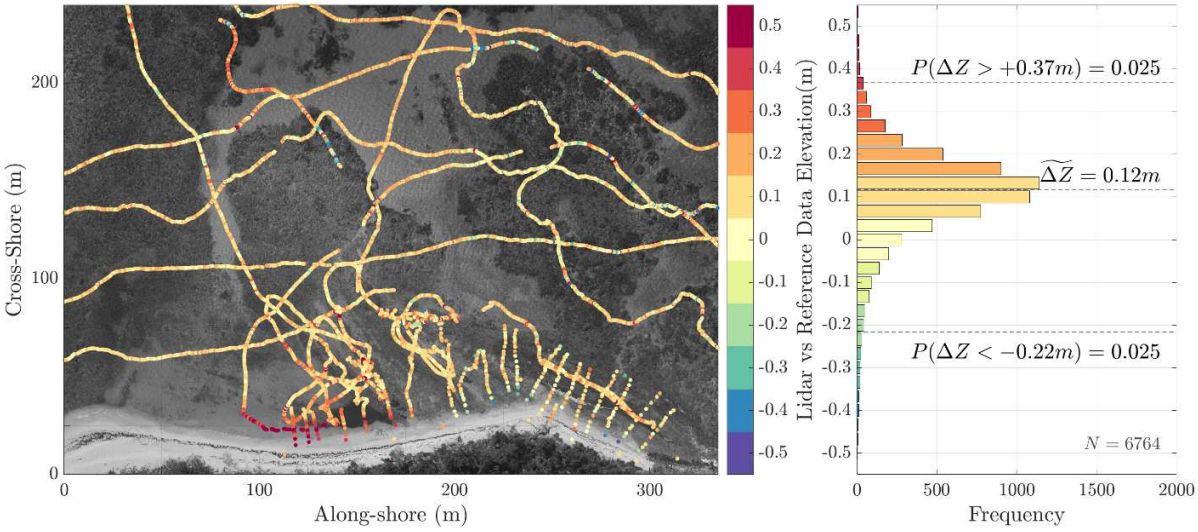

Figure 7. The elevation difference between the bathymetric lidar dataset and the reference dataset, which used a total station and single beam sonar, demonstrates generally good agreement. Note that the total station data are the approximately shore-normal transects close to the shoreline, while the longer tracklines (some roughly shore-parallel) are the sonar data.

4. Results

Data from the two UAS mapping missions were processed using the methodology described in Section 2. For comparison, the data were also processed using the "geometric-only" methodology, which includes only the SfM-MVS bathymetry, with the refraction correction performed as described in Section 2.7

4.1 Geometric-Only Methods

The SfM-MVS point cloud was corrected based on a known water elevation from a nearby tide station and the incident angle from each point to each camera which contains the point within the field of view (Dietrich, 2017). As this method strictly corrects the elevation values of the point cloud based on the viewing geometry and water surface, and does not leverage the radiometric information to fill data gaps, it is referred to as "geometric-only" in the results and discussion section. Figure 8 shows the results of the refraction corrected point cloud for each experiment. Note that for Experiment 2, which was flown at a lower altitude, the SfM-MVS processing was unable to resolve depths for a large portion of the AOI. The larger data gaps in Experiment 2 provided a good test case for investigating the potential to enhance spatial coverage with the combined geometric-radiometric method.

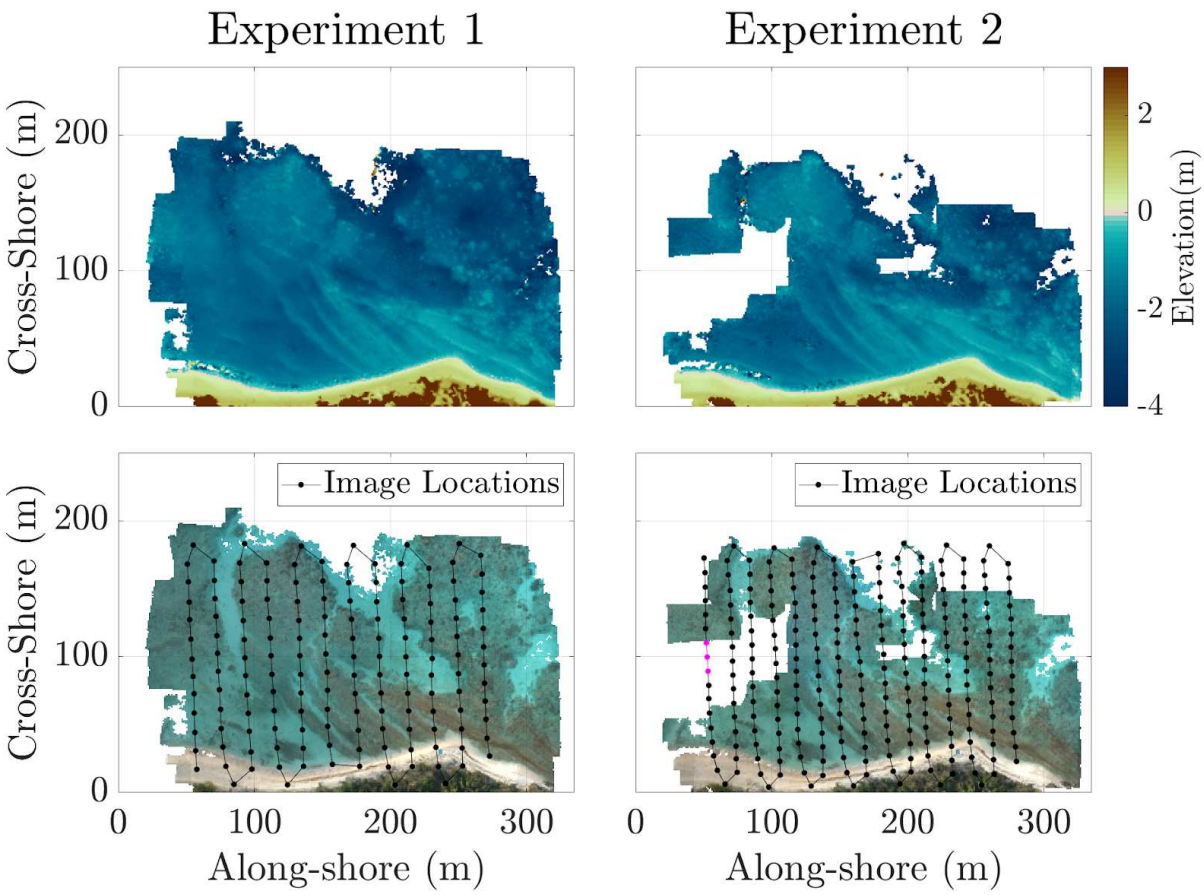

Figure 8. Results of refraction corrected SfM-MVS data for Experiments 1 and 2. Both experiments produced results with data gaps over regions with a texture-less seafloor, though Experiment 2 produced much larger data gaps.

4.2 Radiometric Method Comparison

The geometric-radiometric methods using the four radiometric models described in Section 2.6 and the geometric-only method were all compared to the reference bathymetric lidar dataset. These methods and model names are summarized in Table 2. All data were gridded to a raster with 10-cm cell spacing. The reference data was gridded using a Delaunay triangulation-based TIN-to-grid approach, as the data were sparser, while the data from the radiometric and refraction correction methods were gridded using the average of the values within each grid cell. The DEMs were differenced, such that a positive value indicated a predicted depth that is too shallow when compared to the reference lidar data. Spatial plots of the elevation errors and a histogram of the distribution of errors for each method are shown for Experiments 1 and 2 in Figures 9 and 11 and Figures 10 and 12, respectively. Statistics for the errors of each method are reported in Tables 3-4. All of the error distributions were found to fail normality tests based on skewness and kurtosis, such that error statistics based on the assumption of Gaussian distributions could not be used. Therefore, we computed and reported the following test statistics: 1) the median, and 2) the 95th percentile error, computed following the recommendations and procedures outlined in American Society for Photogrammetry and Remote Sensing (ASPRS) guidelines for lidar vertical accuracy reporting, in the case that error distributions are non-Gaussian (ASPRS, 2004). The 95th

percentile error represents “where 95 percent of errors have absolute values that are equal to or smaller than the specified amount.” Additionally, the percentages of the data with errors of magnitude greater than 0.5 m and 1 m were computed as additional metrics for the width of the distributions. It is important to note in Tables 3-4 that the spatial coverage for the geometric-only processing method is defined relative to the coverage of the geometric-only method. In other words, the 100.0% coverage of the geometric-only method serves as a baseline for evaluating the increased coverage of the geometric-radiometric methods. Finally, the processing times referenced in each of the tables are for a Windows 10 Desktop PC with an Intel Xeon CPU (E5-1603 @ 2.80 GHz), GeForce GTX 980 graphics card (4 Gb), and 32 Gb of RAM.

Table 2. The four models are compared to the geometric-only methodology method.

Model Name	Model Description
Lookup Table	Lookup table using normalized and histogram stretched R,G,B digital numbers
LogRatio	Linear fit to the ratio of the log(B)/log(R)
NN(R,G,B,ISO)	Shallow Neural Network trained with R, G, B, ISO (RGBi) values
NN(All)	Shallow Neural Network trained with (R, G, B, ISO, ΔE, ΔN, time, pixel x, pixel y)
Geometric-only	Point cloud refraction correction methodology proposed by Dietrich (2017)

4.2.1 Experiment 1 Results

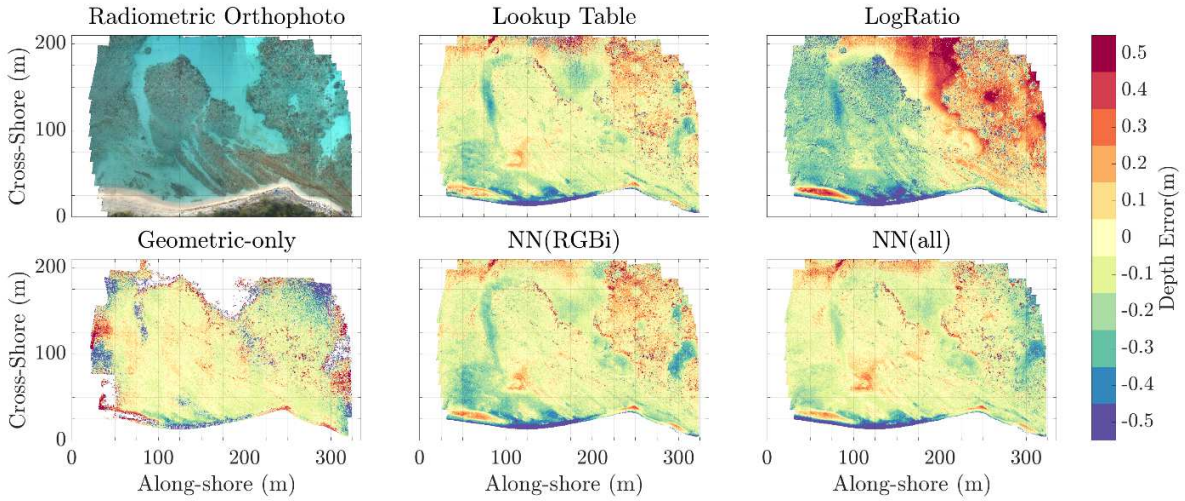

Figure 9. Vertical errors (compared to ground truth lidar data) for each of the models applied to the data from Experiment 1.

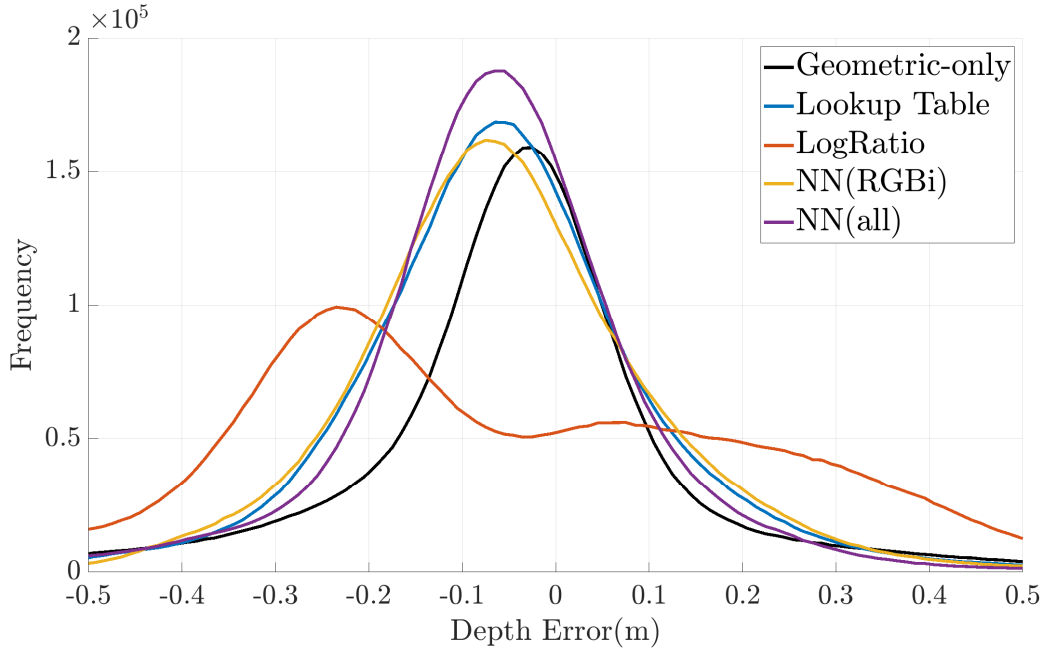

Figure 10. Histogram of depth errors for each of the models applied to the data from Experiment 1.

Table 3. Results of each of the models applied to Experiment 1.

Name	Geometric-Only	Lookup Table	LogRatio	NN(RGBi)	NN(all)
Median (m)	-0.04	-0.06	-0.10	-0.06	-0.06
95th percentile error (m)	0.62	0.39	0.56	0.37	0.37
|Depth Error| > 1m	1.7%	0.2%	0.3%	0.1%	0.1%
|Depth Error| > 0.5m	7.4%	2.7%	7.5%	2.0%	2.3%
Coverage Relative to Geometric-only		+21%	+21%	+21%	+21%
Time to train model (HH:MM:SS)	n/a	0:00:21	0:00:01	1:46:29	0:56:36
Time to apply model (HH:MM:SS)	n/a	1:06:47	1:06:30	2:10:29	3:32:12
Total time (HH:MM:SS)	n/a	1:23:31	1:22:52	4:13:24	4:36:21

4.2.2 Experiment 2 Results

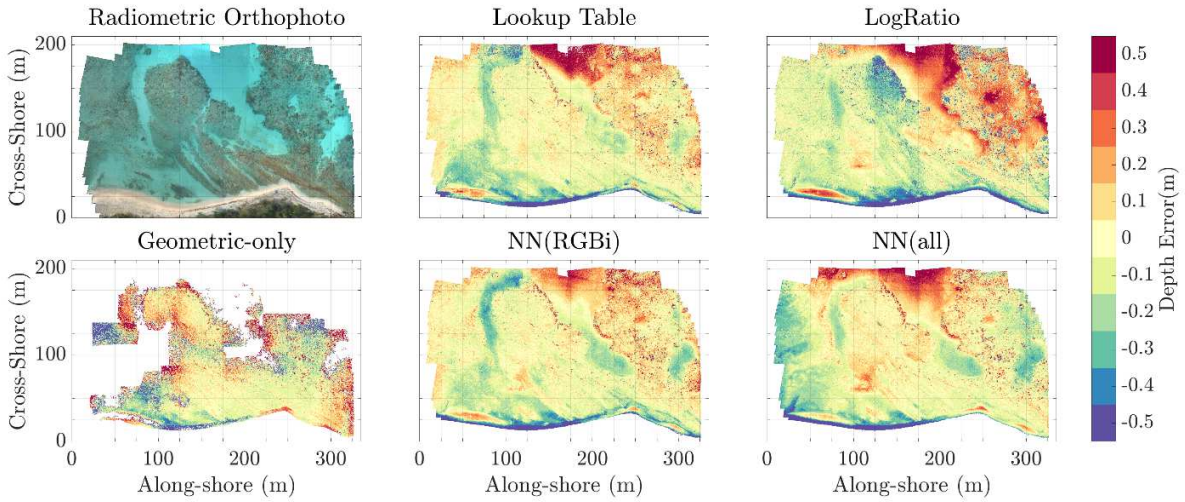

Figure 11. Vertical errors (compared to ground truth lidar data) for each of the models applied to the data from Experiment 2.

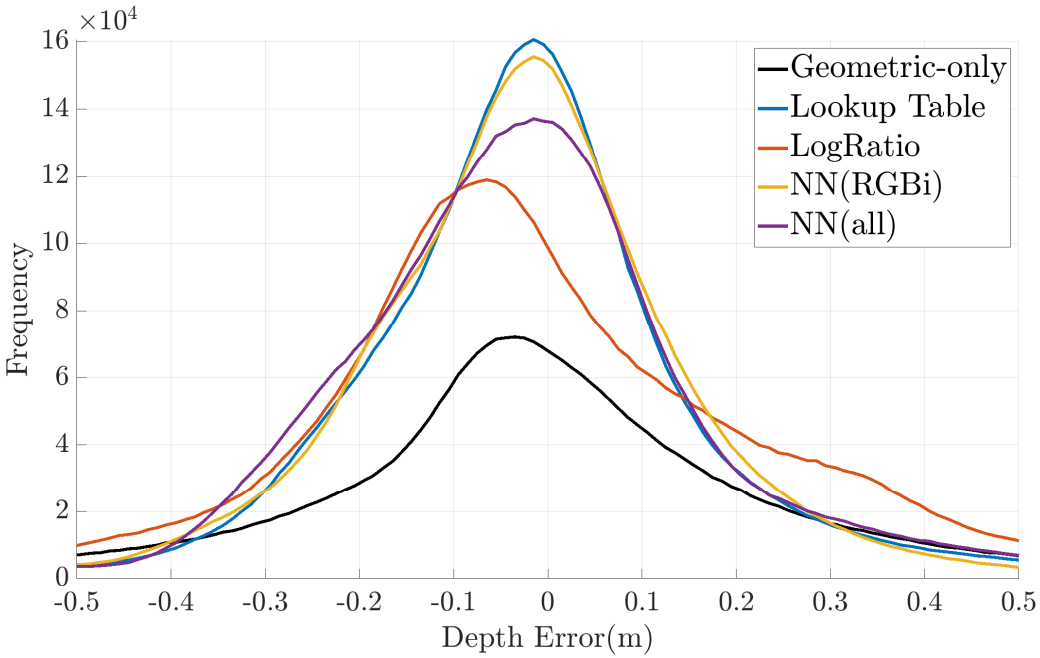

Figure 12. Histogram of depth errors for each model applied to Experiment 2.

Table 4. Results of each of the models applied to Experiment 2.

Name	Geometric-Only	Lookup Table	LogRatio	NN(RGBi)	NN(all)
Median (m)	-0.02	-0.02	-0.04	-0.02	-0.03
95th percentile error (m)	0.77	0.47	0.54	0.39	0.43
|Depth Error| > 1m	2.5%	0.4%	0.3%	0.1%	0.1%
|Depth Error| > 0.5m	12.1%	4.5%	6.6%	2.6%	3.4%
Coverage Relative to Geometric-only		+61%	+61%	+61%	+61%
Time to train model (HH:MM:SS)	n/a	0:00:21	0:00:01	1:46:29	0:56:36
Time to apply model (HH:MM:SS)	n/a	1:06:47	1:06:30	2:10:29	3:32:12
Total time (HH:MM:SS)	n/a	1:23:31	1:22:52	4:13:24	4:36:21

5. Discussion

All of the four radiometric models processed with the geometric-radiometric methods increased the coverage of resolved depths, produced a lower percentage of large errors (except the ratio of logs model), and had a lower 95th percentile error than the geometric-only method.

5.1 Increased Coverage

The coverage in which depths were resolved was increased using the geometric-radiometric methods when compared to the geometric-only method: by 21% and 61% for all of the radiometric models in Experiments 1 and 2, respectively. The geometric-only method produced no data in regions with insufficient seafloor texture and poor viewing geometry at the edges of the AOI. The geometric-radiometric method, however, was able to resolve depths in these regions, as depth can be estimated regardless of viewing geometry and seafloor texture. The 30-cm wide transect shown in Figure 13 demonstrates the advantage of the geometric-radiometric method using the neural network trained on the RGB and ISO when compared to the geometric-only method. Note that the vertical datum for this figure is adjusted so that the water level is at 0 m elevation. Data from both methods have been filtered by computing the mean elevation in 1-cm grid cells (approximately equal to the ground sample distance of the imagery) in order to remove the noise discussed in Section 2.7.

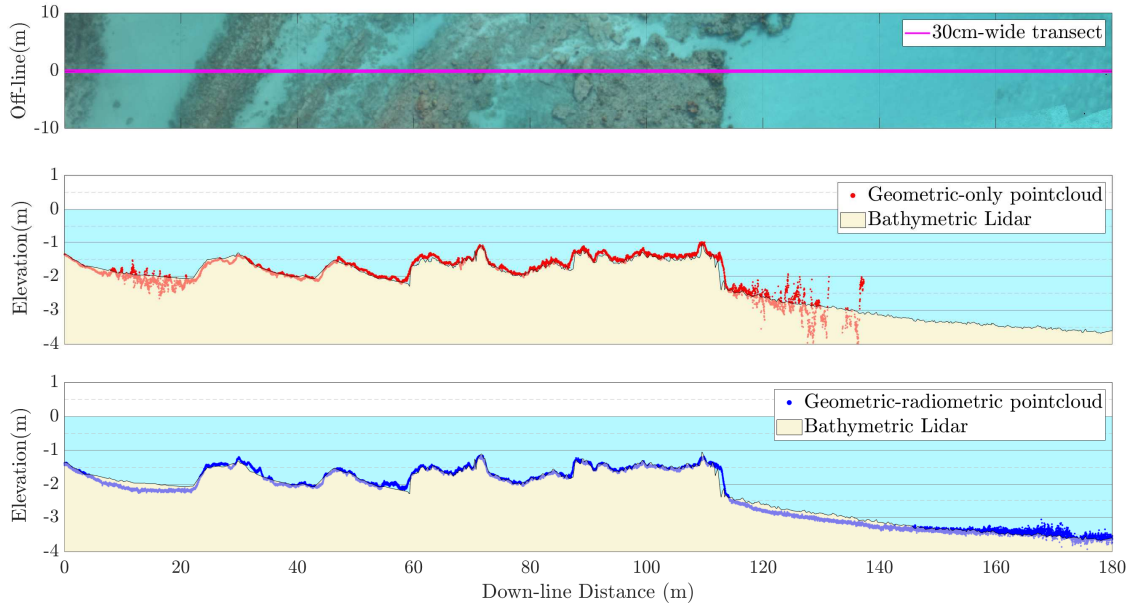

Figure 13. A 30 cm wide transect demonstrates the increased coverage and accuracy of the geometric-radiometric method across a texture-less seafloor. Both the geometric-only and geometric-radiometric data are filtered by computing the average of 1cm bins in the down-line distance.

5.2 Increased Accuracy

As shown in Tables 3 and 4, all of the radiometric models used in the geometric-radiometric method resolved depths with a smaller 95th percentile error than the geometric-only method. Large errors in the geometric-only methods were generally observed in regions with poor texture, where spurious correlations between images adversely affected the SfM-MVS processing. The median between the geometric-only and the geometric-radiometric models varied only slightly between the models, with most differences less than or equal to 3 cm. The log-ratio method in experiment 1, which performed relatively poorly, was the lone outlier with a median depth estimate 2-6 cm deeper than the geometric-only method. Figure 13 demonstrates the improved performance of the geometric-radiometric method in these texture-less regions at 15 m and 130 m in the down-line distance.

Note that there are relatively large vertical errors at the edges of the coral reef, depicted in Figures 9 and 11, as well as in Figure 13 at ~115m down-line distance. This error exists in the geometric-only point cloud and the UAS data is shallower regardless of slope aspect, indicating that it is not due to horizontal uncertainty in the reference data. This error is likely due to either: 1) biases in the refraction correction or 2) uncertainty from the gridded bathymetric lidar being used as the ground truth. Future work will be performed with a more rigorous ground truth dataset to disambiguate these potential error sources.

5.3 Comparison of Models

While the previous section presented the quantitative results of testing the different methods, the analysis performed in this study also enabled a more qualitative assessment of the four different radiometric models, based on the user's experience in implementing and running them. A summary of the main findings is presented here.

The lookup table yielded fast and accurate results, though it produced a slightly higher number of large errors when compared to the other methods. While it was not the case for these experiments, the lookup table method is unable to estimate a depth for a color which is not represented in the training dataset and is, therefore, a poor choice when there is a small training dataset. The log ratio method was fast, but it was consistently the least accurate of the methods. One possible explanation is the lack of robustness to varying illumination of the scene, as is evident in by the visible seam in the spatial elevation error results shown in Figure 9. While this method performed poorly in this experiment, it may prove more advantageous in an experiment where a scene has a minimal training dataset, as the extrapolation and interpolation of data for this model is well-documented in the literature. Both neural network methods were accurate, but took approximately three times longer in total processing time. The accuracy of the interpolation and extrapolation of values which are not present in the training dataset may be unstable due to the nature of neural networks, and should be investigated in future studies. The neural network with all of the features was prone to overfitting the training data, as evidenced by the results at approximately 30 m in the along-shore position and 120 m in the cross-shore position in Figure 11. The geometric-only results are biased deep in this area, causing the neural network with all of the features to generate results that were also too deep in that region.

5.4 Shore-Adjacent Errors

A comparison between the reference data and the lidar data in Section 4 suggested that nearshore erosion/accretion may have occurred in some regions. A comparison between orthophotos generated from imagery acquired coincident with the lidar acquisition and from the UAS data suggests that erosion and accretion occurred near the shoreline between the two surveys in a few areas, as shown in Figure 14. The geometric-only and geometric-radiometric methods both exhibited high elevation errors near the shoreline throughout the AOI where there was: a) active wave breaking and a more variable water surface profile; b) sand changing colors and texture due to wave run-up wetting and drying the beach; and/or c) potential for suspended sediment in the water column. Determination of the extent to which these factors impact the results is complicated by the challenges in decoupling SfM-induced error from real erosion and accretion. We chose not to mask out the data in this region because: 1) it is of interest to investigate how well the different models work in these very shallow regions adjacent to the shoreline where no erosion and accretion have occurred, and 2) the decision of where to mask is highly subjective, and masking all of the data in the nearshore with large errors could artificially improve the reported results.

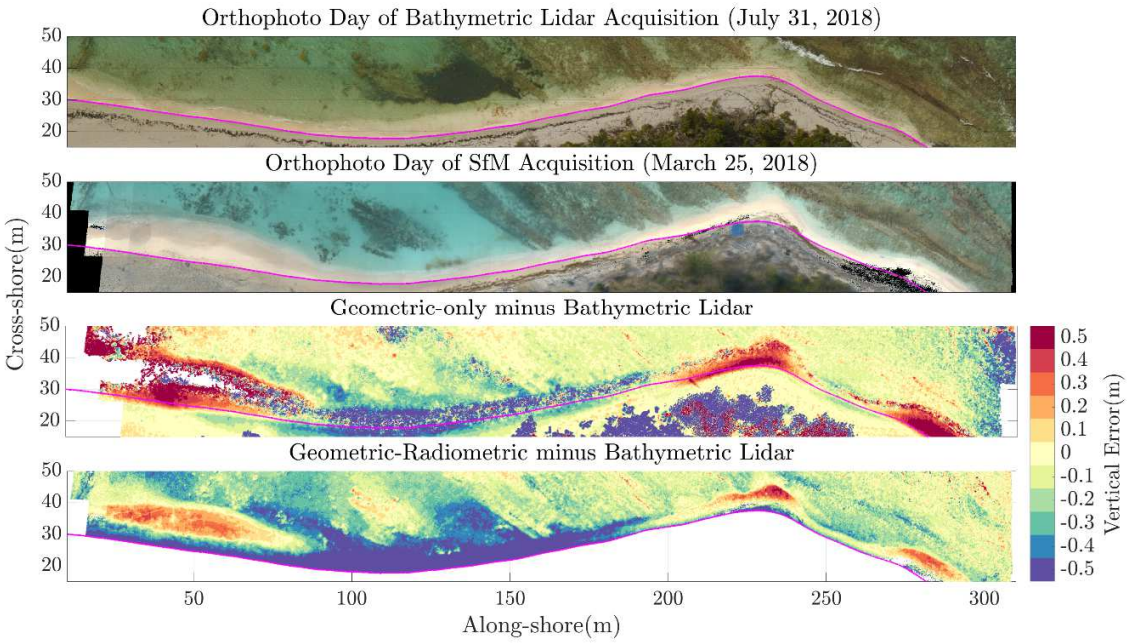

Figure 14. Clear patterns of erosion and accretion occurred between the time of the UAS experiments and the acquisition of the ground truth lidar dataset. Perceived errors in this nearshore region is, in part, due to this real change.

6. Conclusion

This study has demonstrated a novel strategy for combining geometric and radiometric methods of bathymetry retrieval from UAS imagery, with the geometric method consisting of a refraction-corrected SfM-MVS workflow and the radiometric method consisting of multiple spectrally-based depth retrieval (SDB) algorithms. An important finding is that the combination of the two types of approaches greatly increases bathymetric coverage over what is obtained using only the geometric approach. This is primarily due to the fact that the radiometric approaches can estimate depths in homogeneous, featureless areas where the feature matching component of the geometric (SfM-based) methods tends to fail, and also near the edges of the AOI where stereo coverage is reduced. In this study, the increase in coverage was found to be 21% in the first experiment and 61% in the second. Another key finding was that the combined geometric-radiometric approach not only increased coverage, but also accuracy. Comparisons against reference data showed that the 95th percentile error improved (i.e., decreased) by up to 40% in the first experiment and up to 49% in the second. These results confirm the complementary nature of the geometric and radiometric approaches and demonstrate the types of improvements that are achievable through their combination.

While somewhat outside the main objective of the study, ancillary results included the findings of comparing four different radiometric depth retrieval models in the overall geometric-radiometric workflow. These methods included a lookup table, the ratio of logs of two image bands, a shallow neural network trained with RGB and ISO, and a shallow neural network trained using the RGB, ISO, time of image, delta Easting and Northing, and pixel x and y. The shallow neural network trained on the R, G, B and ISO generally provided consistently good results and is recommended for most cases where processing time is not an issue. Importantly, the overall radiometric-geometric approach presented here is

not limited to any particular spectral depth retrieval algorithm, or even to any one particular class of algorithm. The four methods used in this work were merely a representative sampling of available, published approaches, and future work to test additional algorithms in this step is recommended.

One limitation of this approach is that the initial SfM-MVS processing needs to compute accurate depths, camera interior orientation, and camera exterior orientations in order for the radiometric model to be trained and utilized. In both experiments presented here, the SfM-MVS results were found to be sufficient to enable an accurate radiometric model and resultant depth estimates. Additionally, the initial SfM-MVS processing results for both experiments resolved depths across all of the various bottom types within the AOI. For example, the study site in this work contained small patches of sand, which were able to be resolved through SfM-MVS processing, as the coral or other features near the sandy patches provided enough texture to produce a valid (albeit sometimes noisy) depth. This enabled the models to "learn" what the radiometric signature of each seafloor substrate would be in a variety of water depths. The ability of these models to extrapolate and predict depths for substrates which were not resolved through the initial SfM-MVS processing and therefore do not exist in the training dataset should be investigated in future work.

Another important point is that the radiometric models tested in this study are likely sensitive to changing illumination, camera settings and water clarity. Therefore, follow-on work is recommended to investigate the stability of the model parameters across a wider range of project sites and with varying environmental conditions. In particular, it would be of interest to incorporate sites with a wide range of wave conditions and both coastal and inland water types. Incorporating the results of these recommended follow-on studies, the geometric-radiometric bathymetric mapping workflow developed and tested in this work is anticipated to provide a valuable tool for filling shallow-water data voids in many regions around the world, using a cost-effective, UAS-based approach.

Acknowledgements

This work was supported by NOAA's National Centers for Coastal Ocean Science (NCCOS) through a grant to the Cooperative Institute for Marine Resources Studies (CIMRS). The authors thank Tim Battista, Bryan Costa, and Matthew Sharr of NOAA for help with fieldwork and data acquisition. The authors also thank Clayton Pollock and Nathaniel Hanna Holloway at NPS for their field support. The authors also thank USACE JALBTCX for acquiring and processing the bathymetric lidar data which was used as the ground truth dataset for this study.

References

AgiSoft, LLC. Agisoft PhotoScan (1.4.3). Available online: http://www.agisoft.com/downloads/installer/ (accessed March 2018).

ASPRS LiDAR Committee. (2004). ASPRS guidelines vertical accuracy reporting for lidar data. *edited by, LC Flood. http://www* https://www.asprs.org/a/society/committees/lidar/Downloads/Vertical_Accuracy_Reporting_for_Lidar_Data.pdf*)(Accessed: 18 Mar, 2020).*

Brewer, R.K., 1979. Project Planning and Field Support for NOS Photobathymetry. The International Hydrographic Review, 56(2).

Caballero, I., and Stumpf, R. P. (2020). "Towards Routine Mapping of Shallow Bathymetry in Environments with Variable Turbidity: Contribution of Sentinel-2A/B Satellites Mission." Remote Sensing, 12(3), 451.

CloudCompare (version 2.9) [GPL software]. (2019). Retrieved from http://www.cloudcompare.org/

Collins, J., 1979. Cost benefits of photobathymetry. The International Hydrographic Review.

Board, O.S., National Research Council and Mapping Science Committee, 2004. A Geospatial framework for the coastal zone: national needs for Coastal mapping and charting. National Academies Press.

Dietrich, J.T. 2017. Bathymetric structure-from-motion: extracting shallow stream bathymetry from multi-view stereo photogrammetry. Earth Surface Processes and Landforms 42(2): 355-364. DOI: 10.1002/esp.4060

Fonstad, M.A., Dietrich, J.T., Courville, B.C., Jensen, J.L. and Carbonneau, P.E., 2013. Topographic structure from motion: a new development in photogrammetric measurement. Earth Surface Processes and Landforms, 38(4), pp.421-430.

Forfinski-Sarkozi, N.A. and Parrish, C.E., 2019. Active-Passive Spaceborne Data Fusion for Mapping Nearshore Bathymetry. Photogrammetric Engineering & Remote Sensing, 85(4), pp.281-295.

Fryer, J.G. and Kniest, H.T., 1985. Errors in depth determination caused by waves in through-water photogrammetry. *The Photogrammetric Record*, *11*(66), pp.745-753.

Harris, P.T. and Baker, E.K., 2012. Why map benthic habitats?. In *Seafloor geomorphology as benthic habitat* (pp. 3-22). Elsevier.

Harris, W.D. and MJ, U., 1972. Underwater mapping.

Hirschmuller, H., 2007. Stereo processing by semiglobal matching and mutual information. IEEE Transactions on pattern analysis and machine intelligence, 30(2), pp.328-341.

IHO, 2018. Status of Hydrographic Surveying and Charting Worldwide (IHO/OHI Publication C-55). International Hydrographic Organization.

Kotowski, R. (1988). Phototriangulation in multi-media photogrammetry. *International Archives of Photogrammetry and Remote Sensing*, *27*(B5), 324-334.

Legleiter, C. J., Roberts, D. A., Marcus, W. A., & Fonstad, M. A. (2004). Passive optical remote sensing of river channel morphology and in-stream habitat: Physical basis and feasibility. *Remote Sensing of Environment*, *93*(4), 493-510.

Legleiter, C. J., Roberts, D. A., & Lawrence, R. L. (2009). Spectrally based remote sensing of river bathymetry. *Earth Surface Processes and Landforms*, *34*(8), 1039-1059.

Leon, J. X., Phinn, S. R., Hamylton, S. and Saunders, M. I. 2013. Filling the 'white ribbon' – a multisource seamless digital elevation model for Lizard Island, northern Great Barrier Reef. International Journal of Remote Sensing 34(18):6337–6354.

Lyzenga, D.R., 1978. Passive remote sensing techniques for mapping water depth and bottom features. *Applied optics*, *17*(3), pp.379-383.

Lyzenga, D.R., 1981. Remote sensing of bottom reflectance and water attenuation parameters in shallow water using aircraft and Landsat data. *International journal of remote sensing*, *2*(1), pp.71-82.

Lyzenga, D. R., Malinas, N. P., & Tanis, F. J. (2006). Multispectral bathymetry using a simple physically based algorithm. *IEEE Transactions on Geoscience and Remote Sensing*, *44*(8), 2251-2259.

Mandlburger, G. (2019). Through-Water Dense Image Matching for Shallow Water Bathymetry. Photogrammetric Engineering & Remote Sensing, 85(6), 445-455.

Maas, H. G. (2015). On the accuracy potential in underwater/multimedia photogrammetry. *Sensors*, *15*(8), 18140-18152.

Mulsow, C., Kenner, R., Bühler, Y., Stoffel, A., & Maas, H. G. (2018). SUBAQUATIC DIGITAL ELEVATION MODELS FROM UAV-IMAGERY. International Archives of the Photogrammetry, Remote Sensing & Spatial Information Sciences, 42(2).

Murase, T., Tanaka, M., Tani, T., Miyashita, Y., Ohkawa, N., Ishiguro, S., ... & Yamano, H. (2008). A photogrammetric correction procedure for light refraction effects at a two-medium boundary. Photogrammetric engineering & remote sensing, 74(9), 1129-1136.

Meijer, W.O.J.G., 1964. Formula for conversion of stereoscopically observed apparent depth of water to true depth, numerical examples and discussion. *Photogrammetric Engineering*, *30*(10), pp.1037-1045.

Miller, J., Battista, T. A., Pritchett, A. S., Rohmann, S. O. and Rooney, J. J. B. 2011. Coral Reef Conservation Program mapping achievements and unmet needs. US Department of Commerce, National Oceanic and Atmospheric Administration, Coral Reef Conservation Program.

Oborne, Michael, Mission Planner. Available online: https://ardupilot.org/planner/docs/mission-planner-installation.html] (accessed March 2018)

Rinner, K. (1948). *Abbildungsgesetz und Orientierungsaufgaben in der Zweimedienphotogrammetrie*. Österr. Verein f. Vermessungswesen.

Rothermel, M., Wenzel, K., Fritsch, D., & Haala, N. (2012, December). SURE: Photogrammetric surface reconstruction from imagery. In Proceedings LC3D Workshop, Berlin (Vol. 8, No. 2).

Schonberger, J. L., & Frahm, J. M. (2016). Structure-from-motion revisited. In *Proceedings of the IEEE Conference on Computer Vision and Pattern Recognition* (pp. 4104-4113).

Slocum, R.K., W. Wright, C. Parrish, B. Costa, M. Sharr, and T.A. Battista, 2020. Guidelines for Bathymetric Mapping and Orthoimage Generation using UAS and SfM-MVS, An Approach for Conducting Nearshore Coastal Mapping, NOAA Technical Memorandum

Starek, M.J. and Giessel, J., 2017, July. Fusion of uas-based structure-from-motion and optical inversion for seamless topo-bathymetric mapping. In 2017 IEEE International Geoscience and Remote Sensing Symposium (IGARSS) (pp. 2999-3002). IEEE.

Stumpf, R. P., Holderied, K. and Sinclair, M. 2003. Determination of water depth with high-resolution satellite imagery over variable bottom types. Limnology and Oceanography 48(1):547–556.

Tewinkel, G.C., 1963. Water depths from aerial photographs. *Photogrammetric Engineering*, *29*(6), pp.1037-1042.

Westoby, M.J., Brasington, J., Glasser, N.F., Hambrey, M.J. and Reynolds, J.M., 2012. 'Structure-from-Motion' photogrammetry: A low-cost, effective tool for geoscience applications. Geomorphology, 179, pp.300-314.

Woodget AS, Carbonneau PE, Visser F, Maddock IP. 2015. Quantifying submerged fluvial topography using hyperspatial resolution UAS imagery and structure from motion photogrammetry. *Earth Surface Processes and Landforms* 40: 47– 64.

Vanhellemont, Q., and Ruddick, K. (2016). "ACOLITE processing for Sentinel-2 and Landsat-8: atmospheric correction and aquatic applications." 12

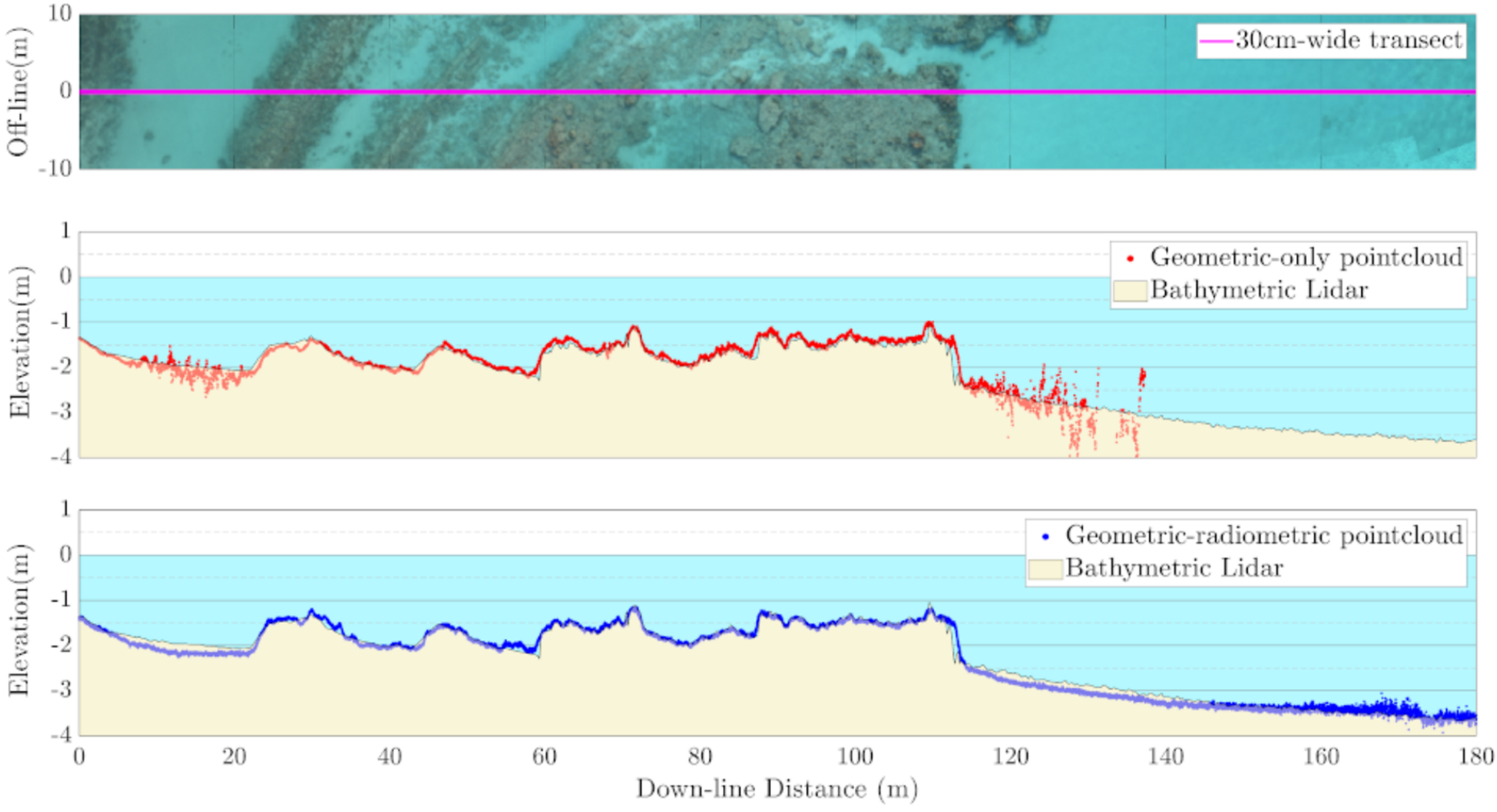
Off-line(m)
10
0
-10
30cm-wide transect
Elevation(m)
1
0
-1
-2
-3
-4
Geometric-only pointcloud
Bathymetric Lidar
Elevation(m)
Geometric-radiometric pointcloud
Bathymetric Lidar
0
20
40
60
80
100
120
140
160
180
Down-line Distance (m)